Electrochemically Induced Cation Disorder and Phase Transformations in Lithium Intercalation Oxides

Yet-Ming Chiang,* Haifeng Wang, and Young-Il Jang

Department of Materials Science and Engineering and Center for Materials Science and Engineering, Massachusetts Institute of Technology, Cambridge, Massachusetts 02139

Received July 13, 2000. Revised Manuscript Received October 17, 2000

Electrochemical cycling of lithium intercalation compounds used as energy storage electrodes often results in phase transformations that have a critical impact on charge capacity and cycle life. In this paper, the role of cation disorder and transformation microstructures on electrochemical performance is examined theoretically and experimentally. The crystallographically allowable domain formation processes for transformations in ordered-rock salt and spinel structure lithium transition metal oxides are discussed. Experimental results from orthorhombic and monoclinic phase $LiMnO_2$ and $Li(Al,Mn)O_2$ materials, the exemplar of compounds that exhibit improved high capacity and stable cycling after electrochemical transformation, are presented. Electron diffraction is used to show that the transformed spinels possess ≈25% cation inversion after extensive cycling. High-resolution electron microscopy reveals that the cycling-induced spinel transformation concurrently creates antiphase domains of ≈6-nm size, which then transform to tetragonal ferroelastic domains upon further lithiation. The respective roles of cation inversion and ferroelastic accommodation in providing cycling stability are discussed. A domain wall sliding mechanism is proposed for the ferroelastic accommodation of transformation strains in this system.

I. Introduction

Lithium and proton intercalation oxides are widely used as storage electrodes in rechargeable battery technology, where performance is largely measured by the ability of the compound to accommodate a large reversible composition change (storage capacity) over a useful voltage range for many intercalation cycles (cycle life). Similar criteria apply to compounds used for electrochromic devices and hydrogen storage. Among lithium intercalation cathodes, for example, approximately one-half of the lithium in $LiCoO_2$[1,2] and $LiNiO_2$[3−5] can be reversibly intercalated, whereas all of the lithium in $LiMn_2O_4$ can be reversibly cycled.[6,7] It is not surprising that a multitude of phase transitions can occur because of the large electrochemically induced composition changes.[1,6−17] Capacity loss upon cycling has generally been attributed to mechanical failure accompanying the phase transitions. One crystal-chemical approach to improving cycling stability seeks compounds with a minimal composition-dependent volume change, exemplified by the "zero-strain" material $Li(Li,Ti)_2O_4$.[18] However, for most intercalation compounds the maximum reversible capacity and cycling fade are determined by the extent to which volume and shape changes accompanying the phase transformations are accommodated at the microscopic level. We earlier reported the existence of antiphase and ferroelastic domains in transformed lithium manganese oxides, which exhibit greatly improved cycling compared to that of conventional $LiMn_2O_4$ spinel, and argued that they provide for strain accommodation during cycling.[19] A direct analogy can be made with the engineered microstructures that have been developed to improve the strength and fracture toughness of transformation-toughened zirconia ceramics,[20] or to optimize the cyclic electromechanical

* To whom correspondence should be addressed.

(1) Reimers, J. N.; Dahn, J. R. *J. Electrochem. Soc.* **1992**, *139*, 2091.
(2) Mizushima, K.; Jones, P. C.; Wiseman, P. J.; Goodenough, J. B. *Mater. Res. Bull.* **1980**, *15*, 783.
(3) Dahn, J. R.; Von Sacken, U.; Juzkow, M. W.; Al-Janaby, H. *J. Electrochem. Soc.* **1991**, *138*, 2207.
(4) Ohzuku, T.; Ueda, A.; Nagayama, M. *J. Electrochem. Soc.* **1993**, *140*, 1862.
(5) Delmas, C.; Saadoune, I.; Rougier, A. *J. Power Sources* **1993**, *43/44*, 595−602.
(6) Thackeray, M. M. *Prog. Solid State Chem.* **1997**, *25*, 1.
(7) Thackeray, M. M. *J. Am. Ceram. Soc.* **1999**, *82*, 3347.
(8) Van der Ven, A.; Aydinol, M. K.; Ceder, G. *J. Electrochem. Soc.* **1998**, *145*, 2149.
(9) Wolverton, C.; Zunger, A. *Phys. Rev. Lett.* **1998**, *81*, 606.
(10) Peres, J. P.; Weill, F.; Delmas, C. *Solid State Ionics* **1999**, *116*, 19.
(11) Delmas, C.; Ménétrier, M.; Croguennec, L.; Levasseur, S.; Pérès, J. P.; Pouillerie, C.; Prado, G.; Fournès, L.; Weill, F. *Int. J. Inorg. Mater.* **1999**, *1*, 11.
(12) Reimers, J. N.; Fuller, E. W.; Rossen, E.; Dahn, J. R. *J. Electrochem. Soc.* **1993**, *140*, 3396.
(13) Gummow, R. J.; Liles, D. C.; Thackeray, M. M. *Mater. Res. Bull.* **1993**, *28*, 1249.
(14) Gummow, R. J.; Thackeray, M. M. *J. Electrochem. Soc.* **1994**, *141*, 1178.
(15) Vitins, G.; West, K. *J. Electrochem. Soc.* **1997**, *144*, 2587.
(16) Kötschau, I. M.; Dahn, J. R. *J. Electrochem. Soc.* **1998**, *145*, 2672.
(17) Shao-Horn, Y.; Hackney, S. A.; Armstrong, A. R.; Bruce, P. G.; Gitzendanner, R.; Johnson, C. S.; Thackeray, M. M. *J. Electrochem. Soc.* **1999**, *146*, 2404.
(18) Ohzuku, T.; Ueda, A.; Yamamoto, N. *J. Electrochem. Soc.* **1995**, *142*, 1431.
(19) Wang, H.; Jang, Y.-I.; Chiang, Y.-M. *Electrochem. Solid-State Lett.* **1999**, *2*, 490.
(20) Heuer, A. H. *J. Am. Ceram. Soc.* **1987**, *70*, 689.

10.1021/cm000569z CCC: $20.00
Published on Web 12/08/2000

response of ferroelectrics.[21] Correspondingly, it may be possible to engineer the microstructure of electrochemically active materials to improve performance. The basic framework for understanding transformation-induced microstructures in intercalation oxides, and their role in strain accommodation, has not previously been elucidated.

This paper has three main objectives. First, we determine from purely crystallographic considerations the types of domain microstructures that can arise when lithium intercalation oxides undergo phase transitions. Prototypical ordered-rock salt and spinel structure lithium transition metal oxides are used as examples. Second, experimental results detailing the cation disorder and microstructural transformations that accompany the cycling-induced spinel transformation in lithium manganese oxides are presented. These compounds represent a class of high-energy density, low-cost cathodes of growing commercial interest. The relative importance of cation inversion and antiphase/ferroelastic domain formation on the cycling stability of this system is considered. Finally, we speculate on the role of phase transformations on cycling stability in other systems where fewer results presently exist.

II. Crystallographic Considerations

A phase transition that is accompanied by symmetry reduction generally results in the formation of a multidomain structure,[22] except in the case of crystallites that are small enough to remain single-domain. Two general classes of domains can be distinguished: ferroic domains and antiphase domains.[23] A crystal is ferroic when it has multiple orientation states in the absence of a field and can be shifted from one to another of these states by the application of a field.[24] Here, the field is magnetic, electric, and mechanical (stress) for ferromagnetic, ferroelectric, and ferroelastic materials, respectively. A ferroic domain is a homogeneous region with a particular orientation state. Therefore, the axis system of adjacent ferroic domains are at least partially nonparallel or antiparallel. On the other hand, antiphase domains have parallel axis systems; neighboring antiphase domains have the same structure and orientation, but are displaced by a translation that is not a symmetry operation of the crystal.[25,26]

One can predict the possible occurrence of ferroic and antiphase domains from group-theoretical considerations.[23,27] There are three types of subgroups defined in crystallographic space groups: (a) *translationengleiche* or *t*-subgroup (retaining the translational elements, but reducing the order of the point group), (b) *klassengleiche* or *k*-subgroup (preserving the point group, but with a loss of translations), or (c) *allgemeine* or general subgroup (loss of translations and reduction in the order of the point group). When the space group of the derived structure is a *k*-subgroup of the space group of the parent structure, only antiphase domains can occur in the derived structure. When the space group of the derived structure is a *t*-subgroup of the parent structure, only ferroic domains are expected. The number of orientation states is determined by the ratio of the orders (number of symmetry elements) of the point groups of the parent and derived structures. Domains that are simultaneously ferroic and antiphase are possible when the space group of the derived structure is a general subgroup of the space group of the parent structure. By considering the symmetry properties of all possible parent-derived space group combinations, Aizu[28] has determined that there are 94 possible ferroelastic species (defined as a combination of a group and subgroup) that exhibit spontaneous strain.

Previously, the formation of domain structures has been studied in the context of temperature- or pressure-induced phase transformations.[23,29] The domain formation process in intercalation compounds is fundamentally different from these in that the phase instability is caused by composition change. That is, the materials of concern here are open systems in which the electrochemically induced phase transition occurs under (to first approximation) isothermal and isobaric conditions. Nonetheless, the same basic crystallographic considerations apply. Below, we consider the phase transitions and possible domain structures that result from the group−subgroup relationship in spinel and ordered-rock salt structure intercalation oxides, represented by the positive electrode materials $LiMn_2O_4$, $LiMnO_2$, $LiCoO_2$, and $LiNiO_2$.

2.1. $LiMn_2O_4$. $LiMn_2O_4$ has the normal spinel structure (space group $Fd\bar{3}m$) in which Mn ions are located on one-half of the octahedral sites (16*d*) and Li ions on one-eighth of the tetrahedral sites (8*a*) within the nearly cubic-close-packed oxygen sublattice (32*e*).[30] Li insertion/extraction occurs on the 8*a* sites at ≈4 V vs Li/Li^+ for $0 < x \leq 1$ in $Li_xMn_2O_4$, while it occurs on the 16*c* sites at ≈2.9 V for $1 < x \leq 2$.[6,7] (In this paper we will use the subscripts *x* and *z* to denote lithium concentration for compounds written with the spinel stoichiometry $Li_xM_2O_4$ and the ordered-rock salt stoichiometry Li_zMO_2, respectively.) As the 16*c* octahedra share faces with the 8*a* tetrahedra, electrostatic interactions between the Li ions on these two sites cause a cooperative displacement of the Li ions on the 8*a* sites into neighboring, vacant 16*c* sites.[6] The lithiated spinel phase with the rock salt stoichiometry $Li_2Mn_2O_4$ has a tetragonal symmetry (space group $I4_1/amd$) due to cooperative Jahn−Teller distortion induced by high-spin Mn^{3+} ($t_{2g}^3e_g^1$).[31,32] The phase transition causes a 5.6% increase in unit cell volume and a 16% increase in the *c*/*a* ratio,[6] resulting in a spontaneous strain. Cubic and tetragonal phases coexist for $1 < x < 2$, and over this concentration range the fraction of tetragonal phase increases with

(21) Jaffe, B.; Cook, J. W.; Jaffe, H. *Piezoelectric Ceramics*; Academic Press: New York, 1971.
(22) Janovec, V. *Ferroelectrics* **1976**, *12*, 43.
(23) Wondratschek, H.; Jeitschko, W. *Acta Crystallogr.* **1976**, *A32*, 664.
(24) Aizu, K. *Phys. Rev.* **1970**, *B2*, 754.
(25) Allen, S. M.; Thomas, E. L. *Structure of Materials*; John Wiley & Sons: New York, 1999.
(26) Wadhawan, V. K. *Phase Transitions* **1982**, *3*, 3.
(27) Burns, G.; Glazer, A. M. *Space Groups for Solid State Scientists*, 2nd ed.; Academic Press: San Diego, CA, 1990.
(28) Aizu, K. *J. Phys. Soc. Jpn.* **1969**, *27*, 387.
(29) Salje, E. K. H. *Phase Transitions in Ferroelastic and Co-elastic Crystals*; Cambridge University Press: Cambridge, 1990.
(30) Sickafus, K. E.; Wills, J. W.; Grimes, N. W. *J. Am. Ceram. Soc.* **1999**, *82*, 3279.
(31) Thackeray, M. M.; David, W. I. F.; Bruce, P. G.; Goodenough, J. B. *Mater. Res. Bull.* **1983**, *18*, 461.
(32) Mosbah, A.; Verbaere, A.; Tournoux, M. *Mater. Res. Bull.* **1983**, *18*, 1375.

overall lithium concentration as dictated by the two-phase equilibrium.

Since $I4_1/amd$ is a maximal nonisomorphic *t*-subgroup of $Fd\bar{3}m$,[33] the formation of ferroelastic domains is possible during the cubic → tetragonal phase transition. The corresponding ferroelastic species according to Aizu's notation[28] is $m\bar{3}m$F4/mmm. (The "F" stands for ferroic, and separates the parent point group ($m\bar{3}m$) on the left from the derived point group (4/mmm) on the right.) As $m\bar{3}m$ and 4/mmm are of the order 48 and 16, respectively, there are 3 possible orientation states (i.e., orientations of *c* axis) in the tetragonal phase. Therefore, the formation of ferroelastic domains, including transformation twinning, is expected during the cubic to tetragonal spinel transformation. However, the formation of antiphase domains is not possible despite the reordering of Li ions from 8*a* to 16*c* sites.

2.2. $LiMnO_2$. $LiMnO_2$ is known to exist in two ordered-rock salt polymorphs, whereby oxygen ions form a nearly cubic-close-packed array in which all octahedral interstices are occupied by an ordered array of Li and Mn ions.[6] The local symmetry around Mn^{3+} is again distorted from a regular octahedron because of the high-spin Mn^{3+}, and the resulting crystal symmetry is either orthorhombic or monoclinic depending on the cation ordering.[34] In orthorhombic $LiMnO_2$ (*o*-$LiMnO_2$, space group $Pmnm$), a view along the ⟨010⟩ direction shows alternating zigzag (corrugated) layers of Li and Mn ions.[35] In monoclinic $LiMnO_2$ (*m*-$LiMnO_2$, space group $C2/m$), Li and Mn ions have the α-$NaFeO_2$ type of cation ordering in which each ion occupies alternate octahedral site layers parallel to the {111} plane of the cubic oxygen sublattice.[36]

Both *o*- and *m*-$LiMnO_2$ irreversibly transform to "spinel-like" structures upon electrochemical cycling, consistent with the appearance of two plateaus at ≈4 and ≈2.9 V vs Li/Li^+.[12−17] As the parent space groups $Pmnm$ and $C2/m$ are subgroups of the $Fd\bar{3}m$ spinel, rather than the other way around, one cannot determine the possible domain structures in the spinel-like phase from the conventional group−subgroup relationship. However, if we hypothesize an intermediate cation distribution giving a space group of higher symmetry than the spinel, domain structures are possible. One such intermediate structure is a disordered rock salt in which only octahedral sites are occupied and in a random distribution. However, because the preferred migration path for Mn ions during the transformation is believed to be via tetrahedral sites,[13] a more likely intermediate structure has Li and Mn ions occupying both octahedral and tetrahedral sites in a disordered distribution. The space group of either of these proposed intermediate structures is most likely $Fm\bar{3}m$. Because $Fd\bar{3}m$ is a nonisomorphic *k*-subgroup of $Fm\bar{3}m$,[33] the formation of antiphase domains is possible during the orthorhombic/monoclinic → spinel transformation. When the transformation is completed after many cycles, the cation ordering will be that of the $LiMn_2O_4$ spinel structure. Figure 1 illustrates the hypothesized transformation of *o*- and *m*-$LiMnO_2$ to spinel. By inspection, the displacement vector across an antiphase domain boundary is expected to be the $^1/_4$<110> of the cubic spinel,[19] as shown in Figure 2. With further lithiation of $LiMn_2O_4$ to tetragonal $Li_2Mn_2O_4$, the formation of ferroelastic domains are possible, as discussed above. The interaction between pre-existing antiphase domain boundaries and later-formed ferroelastic domain boundaries is not obvious a priori, but is revealed in the experimental results discussed later.

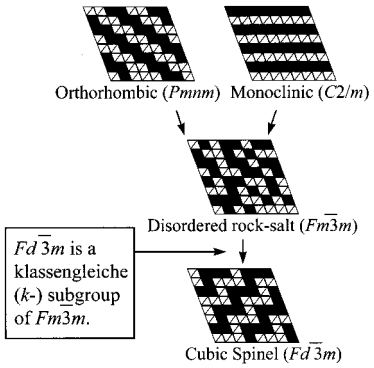

Figure 1. Crystallography of the transformation from *o*- and *m*-$LiMnO_2$ to spinel upon electrochemical cycling.

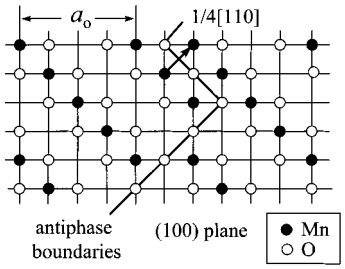

Figure 2. Structure of antiphase domain boundary in $LiMn_2O_4$ spinel. Two ordered spinel domains are displaced relative to one another by the vector ⟨110⟩.

2.3. $LiCoO_2$ and $LiNiO_2$. $LiCoO_2$ and $LiNiO_2$ both have an ordered-rock salt structure with α-$NaFeO_2$-type cation layering, like *m*-$LiMnO_2$.[37,38] This $LiMO_2$ structure is slightly distorted, giving rise to rhombohedral symmetry, space group $R\bar{3}m$, in which Li^+, M^{3+}, and O^{2-} occupy 3*b*, 3*a*, and 6*c* sites, respectively. Extraction of Li creates vacancies, and "ordered vacancy compounds" are formed at certain Li concentrations.[9] For example, at the composition of $Li_{0.5}MO_2$, Li ions are ordered in rows separated by rows of vacancies in the Li layer.[1,10,11,39] The ordering is accompanied by a lattice distortion to a monoclinic unit cell (space group $P2/m$).[10,39] Figure 3 shows the unit cell structures of $LiMO_2$ and $Li_{0.5}MO_2$. The monoclinic phase is stable in a small interval centered at $Li_{0.5}MO_2$ after which the host reverts back to the rhombohedral symmetry of $LiMO_2$ upon further Li extraction.[8]

Because $P2/m$ is an *allgemeine* subgroup of $R\bar{3}m$,[33] both antiphase and ferroelastic domains are possible

(33) International Tables for Crystallgraphy, 3rd ed.; Th. Hahn, Ed.; Kluwer Academic Publishers: Amsterdam, The Netherlands, 1993.
(34) Goodenough, J. B. *J. Phys. Rad.* **1959**, *20*, 155.
(35) Hoppe, R.; Brachtel, G.; Jansen, M. *Z. Anorg. Allg. Chem.* **1975**, *417*, 1.
(36) Armstrong, A. R.; Bruce, P. G. *Nature* **1996**, *381*, 499.
(37) Johnston, W. D.; Heikes, R. R.; Sestrich, D. *J. Phys. Chem. Solid* **1958**, *7*, 1.
(38) Goodenough, J. B.; Wickam, D. G.; Croft, W. J. *J. Phys. Chem. Solid* **1958**, *5*, 107.
(39) Reimers, J. N.; Dahn, J. R.; von Sacken, U. *J. Electrochem. Soc.* **1993**, *140*, 2752.

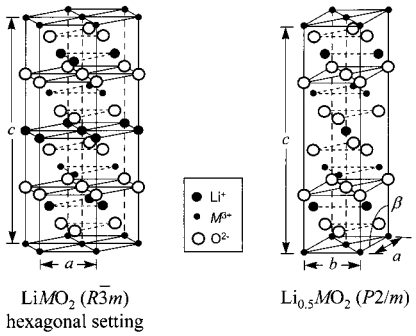

Figure 3. Unit cell structures of $LiMO_2$ (α-$NaFeO_2$ structure type) and the monoclinic ordered vacancy phase $Li_{0.5}MO_2$.

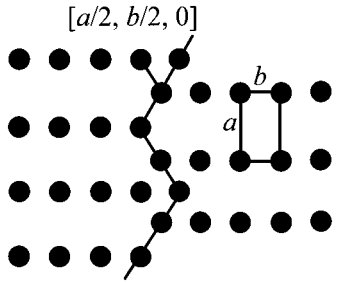

Figure 4. Structure of antiphase domain boundary in $Li_{0.5}MO_2$, viewed in the {*hk*0} plane.

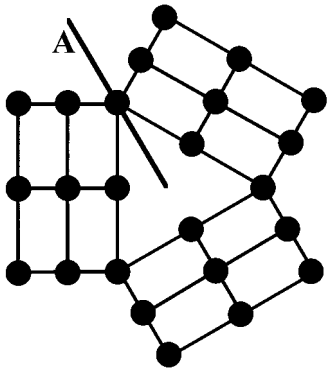

Figure 5. Ferroelastic domain boundary in $Li_{0.5}MO_2$, viewed in the {*hk*0} plane.

upon formation of the monoclinic phase $Li_{0.5}MO_2$. Figure 4 shows a schematic drawing of a Li layer where the antiphase boundary separates two antiphase domains with a diplacement vector of the type ⟨*a*/2, *b*/2, 0⟩ of the monoclinic cell with the *b* axis unique. The ferroelastic species resulting from the rhombohedral → monoclinic transformation is $\bar{3}m$F2/*m*. As $\bar{3}m$ and 2/*m* are on the order of 12 and 4, respectively, three orientation states are possible in the ferroelastic domains that would result in the monoclinic phase. Figure 5 schematically shows a Li layer with these three domain orientations. Note that the boundary *A* is a ferroelastic boundary, but not a twin boundary. As the lost symmetry operation during the phase transformation is $\bar{3}$, the formation of twin boundaries is not possible; twin boundaries are formed only when mirror planes are lost. Considering the Co and O layers, one can clearly see that the boundary A is not a twin boundary (mirror plane). Peres et al.[10] have previously shown the presence of multiple orientations of monoclinic crystallites in the same crystal of Li_zNiO_2 ($0.5 \le z \le 0.75$), consistent with the present discussion. However, their suggestion of a twin structure is not correct from the crystallographic point of view.

Table 1. Space Groups of Well-Known Lithium Intercalation Oxides

crystalline compound	space group
$LiMn_2O_4$	$Fd\bar{3}m$
$Li_2Mn_2O_4$	$I4_1/amd$
o-$LiMnO_2$	$Pmnm$
m-$LiMnO_2$	$C2/m$
$LiMO_2$ (M = Co, Ni)	$R\bar{3}m$
$Li_{0.5}MO_2$ (M = Co, Ni)	$P2/m$
disordered rock salt	$Fm\bar{3}m$

Table 2. Possibilities for Domain Formation upon Phase Transformation in Spinel and Ordered-Rock Salt Lithium Transition Metal Oxides

	phase transformation	antiphase domains	ferroelastic domains
$LiMn_2O_4$	*c*-$LiMn_2O_4$ → *t*-$Li_2Mn_2O_4$	**N**	**Y**
o- and *m*-$LiMnO_2$	*o*- and *m*-$LiMnO_2$ → *c*-$LiMn_2O_4$	**Y**	**N**
	c-$LiMn_2O_4$ → *t*-$Li_2Mn_2O_4$	**N**	**Y**
$LiMO_2$	*rh*-$LiMO_2$ → *m*-$Li_{0.5}MO_2$	**Y**	**Y**
(M = Co, Ni)	*m*-$Li_{0.5}MO_2$ ← *h*-$Li_{0.3}MO_2$	**Y**	**Y**

Tables 1 and 2 list the space groups and possible domain structures in $LiMn_2O_4$, $LiMnO_2$, $LiCoO_2$, and $LiNiO_2$. These examples constitute but a small fraction of the compounds and space groups that comprise crystalline electrochemical storage materials. Nonetheless, they illustrate that antiphase and ferroelastic domains can be widely expected to form during cycling-induced phase transformations. The specific possibilities in each instance are readily determined from the above considerations.

III. Experiments in Lithium Manganese Oxides

The lithium manganese oxides are of particular interest because of the phase transformations discussed in sections 2.1 and 2.2, both of which have important influences on the electrochemical properties of this class of cathodes. $LiMn_2O_4$ is known to undergo rapid capacity fade when it is cycled through the cubic-tetragonal transformation (onto the 3-V plateau), whereas orthorhombic and monoclinic $LiMnO_2$ are known for retaining a high charge capacity despite the transformation to spinel.[12−16,19,40,41] In this work we studied the transformed microstructures of three cathode materials, *o*-$LiMnO_2$, *o*-$LiAl_{0.05}Mn_{0.95}O_2$, and *m*-$LiAl_{0.05}Mn_{0.95}O_2$, the synthesis procedures and electrochemical characterization of which have been described in previous papers.[40−42] All had been extensively cycled (50 to >100 cycles) between 2 and 4.4 V at rates ranging from 26 to 150 mA/g to attempt completion of the electrochemically induced spinel transformation. The final few cycles were conducted at low rates (3.3−7.5 mA/g oxide) and terminated in the fully discharged state (2.0 V) to achieve a nearly fully lithiated oxide. The detailed cycling conditions of the *o*-$LiMnO_2$ and *o*-$LiAl_{0.05}Mn_{0.95}O_2$ samples are shown in refs 41 and 40, respectively. The early cycling data for the *m*-$LiAl_{0.05}Mn_{0.95}O_2$ sample is shown in Fig. 4 of ref 40; it was additionally cycled to 73 cycles at 26.1 mA/g and the

(40) Chiang, Y.-M.; Sadoway, D. R.; Jang, Y.-I.; Huang, B.; Wang, H. *Electrochem. Solid-State Lett.* **1999**, *2*, 107.
(41) Jang, Y.-I.; Huang, B.; Wang, H.; Sadoway, D. R.; Chiang, Y.-M. *J. Electrochem. Soc.* **1999**, *146*, 3217.
(42) Jang, Y.-I.; Huang, B.; Chiang, Y.-M.; Sadoway, D. R. *Electrochem. Solid State Lett.* **1998**, *1*, 13.

last two cycles conducted at 6.5 mA/g. The lithium concentration z in $Li_zAl_yMn_{1-y}O_2$ ranged from 0.81 to 0.97 on the basis of the final discharge capacity values of 223−272 mA h/g.[19]

Electron microscopy samples were prepared by ultrasonically deagglomerating the cathode pellets and dispersing onto carbon-coated copper grids. To identify the phase and extent of cation inversion, selected area diffraction (SAD) patterns were taken from thin sections on the edges of the oxide particles. The typical oxide size was 0.5−1.0 μm. A JEOL-2010 high-resolution TEM equipped with a double-tilt sample holder was used to obtain zone-axis diffraction patterns. Diffraction intensities were measured using a Gatan MultiScan CCD camera (MSC). The large dynamic range of the CCD camera allowed simultaneous measurement of strong and weak diffraction spots with a typical signal-to-background ratio between 50 and 200.

To reveal the nanodomain structure of the transformed spinel, a Fourier-filtered imaging technique was used. The HREM images of interest were taken along the spinel cubic ⟨100⟩ and ⟨111⟩ or tetragonal ⟨111⟩ zone axes. Areas of interest in the digitized image were fast-Fourier-transformed (FFT) to obtain a power spectrum, which is equivalent to the selected area diffraction pattern from the same region. Then, a mask was applied to the power spectrum to admit only certain reflections. For images taken along the cubic ⟨111⟩ the strong {440} principles and weak {220} reflections due to cation inversion were isolated. For images along the tetragonal ⟨111⟩, the {011}, {220}, {121}, {123}, and {224} principle reflections were admitted. Weaker higher order reflections, the central transmitted beam, and the noisy background were thereby excluded from the power spectra. The modified power spectra were then subjected to an inverse FFT to obtain the filtered image in which lattice planes and defects are highlighted because the background noise is removed. In addition, the *d*-spacing within individual nanodomains could be obtained from the reciprocal spacing of reflections in the power spectrum of an isolated domain.

The multislice model was used to simulate electron diffraction patterns and diffraction intensities as a function of sample thickness for a series of cubic spinel model structures. The simulated structures included the normal spinel structure (Li on all 8*a* tetrahedral sites), the inverse spinel structure (Mn on all 8*a* tetrahedral sites), and partially inverse spinel structures with varying distributions of Mn and Li on the 8*a* tetrahedral sites.

The sample thickness is an important variable in the comparison between experimental results and simulation. We used two empirical methods to determine the thickness of the thin sections where SAD patterns were taken. One was a combination of convergent beam electron diffraction (CBED) and calculation of extinction distance. The oxide particles studied usually had irregular thickness profiles and a steep thickness gradient at the edges. Only thin, relatively flat, and undistorted edges were selected for analysis. The CBED patterns showed no Kossel−Möllenstedt (K−M) fringes in the CBED spots, which indicated that the thickness of the observed thin sections was less than one extinction distance. The extinction distance, which corresponds to the sample thickness where the first dark band of thickness contours in a bright field image is located, was calculated to be 176 nm for cubic spinel based on the lowest order Bragg reflection. Assuming a linear variation of sample thickness with distance from the particle edge, the spacing between the first thickness contour and the analyzed sections indicated a thickness of about 1/20th of the extinction distance where the SAD patterns were taken or ≈9 nm.

The second method for estimating thickness was based on the highest order of the principle reflections that are observable in SAD. We simulated the diffraction patterns for a range of thicknesses and compared the highest order principle reflections that were detectable to the experimental SAD patterns. The observed patterns usually had 3−4 orders of principle reflections, regardless of the state of cation disorder. In a comparison with the simulations, this indicated sample thicknesses in the range 3−10 nm. The two estimates of sample thickness are in good agreement in that they show the sample thicknesses to be <10 nm in the regions analyzed.

Other factors that could cause variations to the diffraction intensity were also considered. The simulation was simplified by assuming no beam tilting. Experimentally, low index zone axis patterns were obtained by tilting the sample and aligning the zone axis as closely as possible with the incident beam and by averaging the diffraction intensities of several such patterns. The effect of electron scattering from the ≈10-nm-thick amorphous carbon film supporting the oxide particles was not included in the calculation of diffraction patterns and intensities. This was justified from the observation that scattering of the 200-keV electrons from the film alone yielded negligible angular diffuse intensity around the incident beam. Finally, multiple reflections were not included in the simulation.

IV. Results

4.1. Overall Phase Analysis. Electrochemical tests of these samples after the cycling-induced transformation showed clear 4- and 2.9-V plateaus characteristic of lithium manganese spinel.[40,41] The nearly flat 2.9-V plateaus indicate a field of two-phase coexistence[6] across which the fraction of spinel phase with octahedral site (16*c*) Li occupancy increases with increasing lithiation (discharge). The nearly complete lithiation ($z \sim 1$) indicated by the final discharge capacity and the low final discharge voltage of 2.0 V would normally indicate the presence of a single tetragonal spinel phase. However, in the transformed samples this was not found to be the case. We distinguished between the cubic and tetragonal spinel on the basis of the *c*/*a* value measured from selected-area electron diffraction patterns (Figure 6). While less statistically significant than bulk X-ray diffraction of a powder sample, the TEM analysis allows investigation of individual particles. The determination of tetragonality, being limited by the precision to which diffraction spot positions can be measured, is ≈2% of the *c*/*a* ratio. Thus, particles showing $c/a < 1.02$ in selected area diffraction were considered to be cubic, while those with $c/a > 1.02$ were considered to be tetragonal. (The tetragonal spinel is usually described with a unit cell in the *I* setting in which a_0 corresponds to the ⟨110⟩ and c_0 the ⟨100⟩ of the parent cubic spinel (*F* setting), giving $c/a > 1$ even in the case of an undistorted cubic spinel. For simplicity, here, we use the *c*/*a* ratio relative to the cubic spinel lattice, whereby $c/a = 1$ is the ideal cubic phase and $c/a = 1.163$ is the ideal tetragonal phase.[6]) As listed in Table 3, the electron diffraction data for a total of 63 particles showed the following distribution. A relatively large number of observations of cycled *o*-Li_zMnO_2 showed that about 60% of the observed particles was of the cubic spinel phase. Fewer observations of *o*-$Li_xAl_{0.05}Mn_{0.95}O_2$ and *m*-$Li_xAl_{0.05}Mn_{0.95}O_2$ showed approximately equal fractions of cubic and tetragonal spinel.

The results are qualitatively consistent with powder X-ray diffraction previously conducted on the same cycled cathodes. A larger fraction of cubic or low tetragonality spinel (broadened X-ray peaks make the two difficult to distinguish) was observed in the undoped *o*-$LiMnO_2$, and predominantly tetragonal spinel was observed in both aluminum-doped compositions after cycling.[40,41] The limited number of observations do not allow a precise determination of phase fractions. However, compared to conventional $LiMn_2O_4$ spinel, the

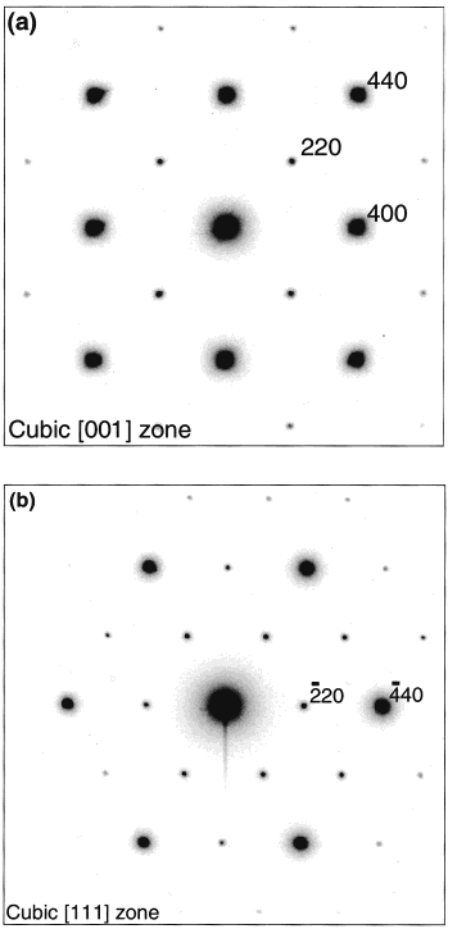

Figure 6. Selected area diffraction patterns for cubic spinel (c/a<1.02) particles in cycled *o*-$LiMnO_2$. Note the appearance of {220} reflections in both (a) [100] and (b) [111] zone axis diffractions, which are indicative of increased scattering from 8*a* tetrahedral sites.

Table 3. TEM Analysis of Spinel Phases in Cycled Lithium Manganese Oxide Cathodes

sample	total number of particles examined	cubic spinel (c/a increase < 2%)	tetragonal spinel (c/a increase ~3−16%)
o-$LiMnO_2$	36	21	15
o-$LiAl_{0.05}Mn_{0.95}O_2$	11	6	5
m-$LiMn_{0.05}Mn_{0.95}O_2$	16	8	8

surprising result in these materials is that a substantial fraction of cubic spinel persists at such high lithiation.

4.2. Extent of Cation Inversion. Typical SAD patterns for transformed spinel of <2% tetragonality are shown in Figure 6 for the ⟨100⟩ and ⟨111⟩ poles. The increased intensity of the {220} diffraction spots relative to $LiMn_2O_4$, arising from the large difference in the atomic scattering factor between Li and Mn ions, is evidence for cation retention on the ordered 8*a* tetrahedral sites in the transformed spinel structure.[19,41] Although powder X-ray diffraction has been previously used to determine the extent of cation inversion in other spinels from the relative intensity of the {220} reflection,[43] in the present samples this is not feasible because of the high background intensity from other components of the cathode mixtures.[41] However, the {220} intensity is easily detected in SAD from single particles.

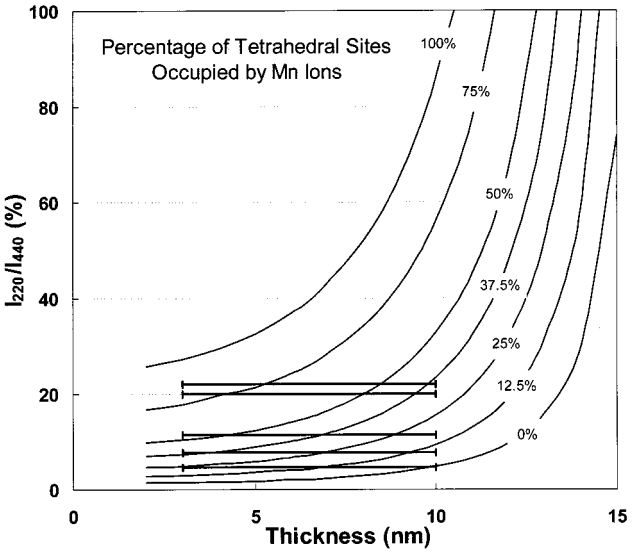

Figure 7. Calculated electron diffraction intensity ratio of {220} and {440} reflections as a function of cation inversion and specimen thickness, compared with experimentally measured intensities (horizontal bars), for specimens of 3−10-nm thickness. Results indicate a significant and variable degree of cation inversion, exceeding 25% in some regions of the oxide.

To quantify the site distribution, we use the relative intensity of {220} and {440} reflections to determine the cation inversion parameter *i*, according to the established convention for spinels[43,44] whereby *i* represents the fraction of tetrahedral sites in an AB_2O_4 spinel that is occupied by B cations. For $LiMn_2O_4$, the corresponding site occupancies of a partially inverse spinel are as follows:

$$(Li_{1-i}Mn_i)_{8a}[Mn_{2-i}Li_i]_{16d}O_4 \qquad (1)$$

Figure 7 shows the calculated I_{220}/I_{440} ratio as a function of sample thickness, for normal, inverse, and partially inverse cubic spinel with varying cation inversion parameters. In normal spinel, the low scattering factor of Li ions on ordered tetrahedral sites results in very weak {220} reflections at thicknesses <10 nm. A systematic increase in the {220} intensity results as Mn is substituted for Li on the tetrahedral sites (in the simulation the remaining Mn and Li randomly cooccupy the ordered octahedral sites, as is usually assumed for the inverse spinel structure). The I_{220}/I_{440} ratio reaches its maximum value for complete inverse spinel ordering ($i = 1$). Experimental measurements of I_{220}/I_{440} ratio in five randomly selected cubic spinel regions in the transformed *o*-$LiMnO_2$ are plotted as horizontal bars, spanning the estimated thickness range of 3−10 nm. All show higher {220} intensity than expected for a normal $LiMn_2O_4$ spinel, indicating at least 10% cation inversion ($i = 0.1$) in every instance. In the two particles exhibiting the highest {220} intensities in Figure 7, comparison with the simulations indicates $i = 0.25-0.75$. On a volume-averaged basis, the extent of cation inversion within this transformed

(43) Datta, R. K.; Roy, R. *Am. Mineral.* **1968**, *53*, 1456; *J. Am. Ceram. Soc.* **1967**, *50*, 578.

(44) Navrotsky, A.; Kleppa, O. J. *J. Inorg. Mater. Chem.* **1967**, *29*, 2701.

spinel is $i \sim 0.25$. A variation in inversion between individual transformed powder particles is not surprising because at normal charge/discharge rates the local electrochemical cycling conditions vary within a composite cathode. Varying extent of cycling-induced damage, including spinel ordering, has been observed among particles in $LiCoO_2$ cathodes.[45,46]

Another measure of the extent of cation inversion is provided by the electrochemical tests. Because the maximum allowable concentration of 8*a* lithium ions is reduced from 1 to $(1 - i)$ when there is cation inversion (eq 1), it is expected that the capacity on the 4-V plateau, which is due to tetrahedral site Li, will be $(1 - i)/1$ times the ideal value.[41] The maximum 4-V capacity assuming complete 8*a* Li occupancy is 50% of the theoretical capacity of $LiMnO_2$ or 142.77 mA h/g. Figure 12 of ref 41 and Figure 4 of ref 40 show the final, low-rate discharge curves for transformed *o*-$LiAl_{0.05}Mn_{0.95}O_2$ and *o*-$LiMnO_2$, respectively. Note that, for both, the capacity of the 4-V plateau measured between 3.4 and 4.4 V is ≈110 mA h/g, which corresponds to having $i = 0.23$, in good agreement with the extent of cation inversion determined by electron diffraction.

4.3. Transformation Microstructures. Figure 8 shows bright field and Fourier-filtered images of a nanodomain structure that is characteristic of cubic spinel regions in the cycled samples (this particular image is from the cycled *o*-$LiMnO_2$). The average lateral dimension of the domains is ≈6 nm, and nearly all of the boundaries between nanodomains are coherent (i.e., the lattice planes are continuous across the boundary). Careful inspection showed that only a few of the boundaries in Figure 8 are incoherent. A higher magnification lattice image (Figure 9) shows contrast across a coherent boundary whereby the lattice fringes in two nanodomains are shifted relative to one another in the ⟨110⟩ direction, as expected for an APB in the spinel structure (Figure 2). Furthermore, as the arrows show, the lattice fringes in two adjacent nanodomains are shifted relative to one another by one-half of a lattice fringe spacing. Because phase contrast lattice fringes such as these result from coherent interference between Bragg diffracted beams, in the spinel structure, a ⟨110⟩ relative shift of the two nanodomains corresponds to a 2π phase shift of the diffracted intensity, which would give rise to no contrast difference across the boundary. However, a ⟨110⟩ displacement of the two nanodomains would cause the lattice fringes intensities to be π out of phase, such that the bright intensity in one domain would align with the dark in the adjacent domain. This is as seen in Figure 9. Thus, we conclude that the electrochemical-cycling produced microstructure consists of antiphase domains in which the APBs have the displacement vector shown in Figure 2.

In regions that selected area diffraction showed to be tetragonal phase spinel, we find a nanostructure that is somewhat coarser than the antiphase domains and in which virtually all domain boundaries are now incoherent (Figure 10). Tetragonality is induced within the earlier-formed antiphase domain pattern without creating new interfacial area. The lattice planes in Figure 10 are of $\{0\bar{1}1\}$ type, and having mixed *k* and *l* indices allows the local tetragonality (*c*/*a*) within each domain to be directly measured from the fringe spacing. These have been labeled in Figure 10. We find that nearly cubic nanodomains (*c*/*a* as low as 1.03) coexist with tetragonal domains that vary widely in *c*/*a*, reaching a maximum value of 1.13. In all cases, however, the tetragonality is less than the limiting value of 1.16 seen in bulk tetragonal $Li_2Mn_2O_4$ (reference). It is notable that a range of *c*/*a* ratios exist, which is unlike the behavior of conventional $LiMn_2O_4$ on the 2.9-V plateau, where two-phase equilibrium between cubic $LiMn_2O_4$ and tetragonal $Li_2Mn_2O_4$ allows *c*/*a* ratios of 1 and 1.16 only.

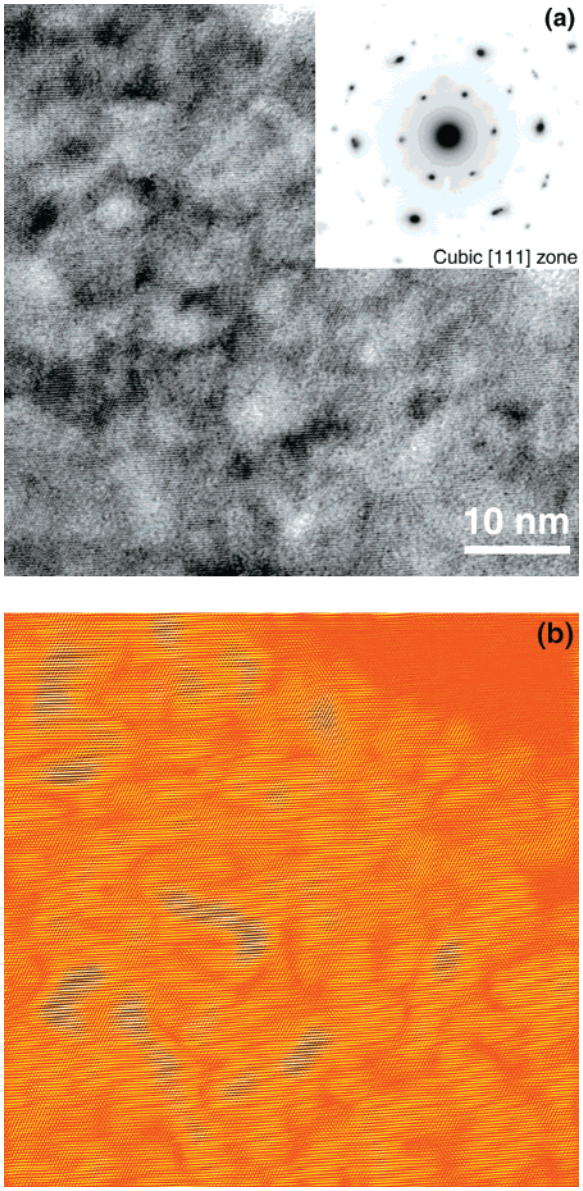

Figure 8. Bright field (a) and Fourier-filtered (b) HREM images of the antiphase domain structure in cubic spinel transformed from *o*-$LiMnO_2$ by electrochemical cycling.

These nanodomains can be classified as ferroelastic domains because they form concurrently with the symmetry-reducing cubic → tetragonal phase transformation discussed in section 2.1. The pre-existing APBs

(45) Wang, H.; Jang, Y.-I.; Huang, B.; Sadoway, D. R.; Chiang, Y.-M. *J. Electrochem. Soc.* **1999**, *146*, 473.
(46) Wang, H.; Jang, Y.-I.; Huang, B.; Chiang, Y.-M.; Sadoway, D. R. *J. Power Sources* **1999**, *81*−*82*, 594.

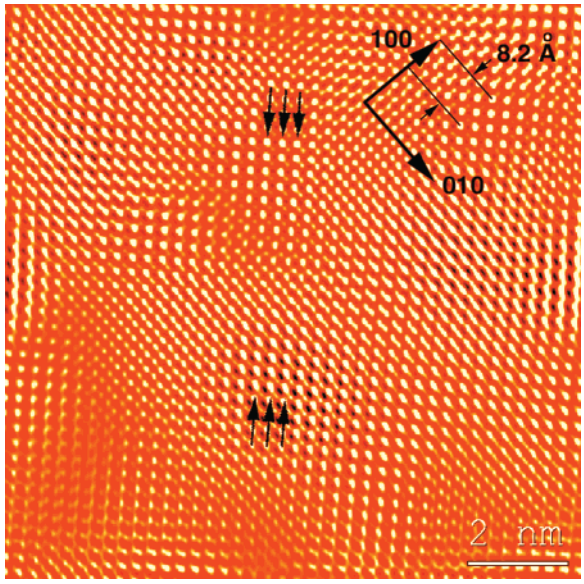

Figure 9. Antiphase domain boundary in cubic transformed spinel. See text for interpretation.

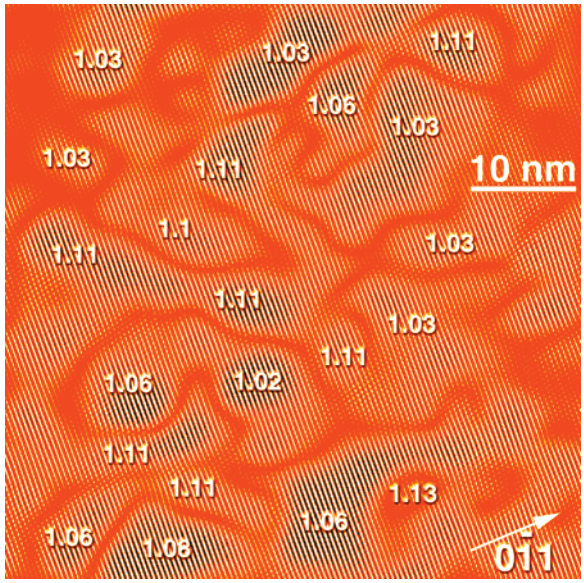

Figure 10. Fourier-filtered HREM image of tetragonal spinel transformed from *m*-$LiAl_{0.05}Mn_{0.95}O_2$. Lattice planes of {0−11} type are visible, from which the *c*/*a* ratio of each tetragonal spinel nanodomain is labeled. Note the wide variation in tetragonality between nanodomains and the highly defective (incoherent) domain boundaries.

appear to be preferred sites for defect formation at which grain boundary dislocations are created to accommodate the crystallographic strain between nanodomains varying in unit cell volume, tetragonality, or orientation. The pre-existing nanodomain morphology precludes the formation of planar transformation-twin boundaries, which are otherwise nearly ubiquitous in ferroelastic materials.[29] Domains misoriented by ≈90°, which commonly form in ferroelastic materials as a mechanism for accommodating local strain while minimizing macroscopic strain, are also not observed. While individual tetragonal domains do occasionally show a slight rotation with respect to one another of a few degrees, there is a predominant texture to the tetragonal nanodomains, which is seen in the streaking of the

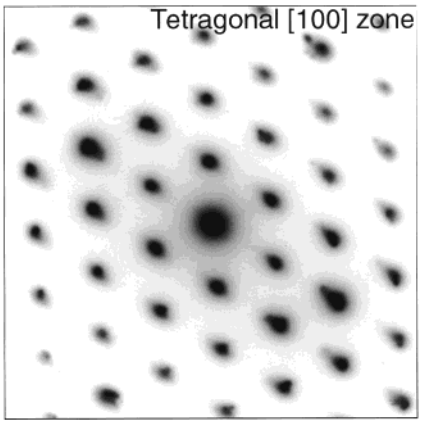

Figure 11. Selected area diffraction pattern of tetragonal spinel region in *o*-$LiAl_{0.05}Mn_{0.95}O_2$, showing streaking of spots indicative of a preferred orientation (texture) as well as variable tetragonality in the nanodomain structure.

SAD pattern (Figure 11). As discussed later, this probably results from a mechanical bias field imposed during electrochemical cycling due to the coupling between concentration gradients and stress.

V. Discussion

The present results show that the electrochemical cycling-induced transformations of *o*- and *m*-$LiMnO_2$ to spinel are accompanied by both *cation disorder* and *microstructural disorder*. The transformed spinels not only have a globally reduced tetragonality at high lithiation compared to $Li_2Mn_2O_4$ but also possess a unique nanodomain microstructure created by cycling. Either, or both, may contribute to the improved cyclability of the transformed spinels compared to conventional $LiMn_2O_4$ cathodes of the normal spinel structure. Below, we consider the respective roles that cation inversion and the formation of antiphase/ferroelastic nanodomains can play in this process.

5.1. Role of Cation Inversion. The transformation of *m*- and *o*-$LiMnO_2$ to perfect spinel ordering requires displacement of 25 and 50% of the Mn ions, respectively, to octahedral sites vacated by the extraction of Li ions. The observation that a significant fraction of the Mn ions remain on tetrahedral sites, forming a partially inverse spinel, supports the model proposed by Gummow et al.[13] for the orthorhombic phase, whereby Mn ions migrate via neighboring tetrahedral sites. In a partially inverse $Li_xMn_2O_4$ spinel, the collective migration of tetrahedral ions from *8a* to *16c* octahedral sites that occurs in normal spinels for $x > 1$ cannot be complete; some disorder remains. The question then arises as to whether cation inversion alone, in the absence of microstructural disorder, can influence the phase transition in a manner beneficial to cycling stability. We can conceive of two general effects:

(1) Cation inversion will alter the phase diagram. The miscibility gap in the region $1 < x < 2$ is of particular interest. First-principles calculations for $LiMn_2O_4$ spinel without cation inversion indicates that, at room temperature, nearly stoichiometric $LiMn_2O_4$ and slightly lithium-deficient $Li_2Mn_2O_4$ coexist in this regime.[47]

(47) Van der Ven, A.; Marianetti, C.; Morgan, D.; Ceder, G. *Solid State Ionics* **2000**, *135*, 21.

Table 4. Jahn−Teller Distortion for Mn Ions as a Function of Valence and Site[a]

ion	site	J−T distortion	induced tetragonality
Mn^{3+}	oct. ($t_{2g}^3e_g^1$)	**Y**	$c/a > 1$
	tet. ($e^2t_2^2$)	**Y**	$c/a < 1$
Mn^{4+}	oct. (t_{2g}^3)	**N**	none
	tet. ($e^2t_2^1$)	**Y**	$c/a > 1$
Mn^{2+}	oct. ($t_{2g}^3e_g^2$)	**N**	none
	tet. ($e^2t_2^3$)	**N**	none

[a] After ref 48.

Lithiation of $LiMn_2O_4$ causes a first-order phase transition to the latter phase, accompanied by a 5.6% volume expansion and 16.3% increase in the *c*/*a* ratio.[6] Above the miscibility gap (calculated to be at ~450 K), however, a continuous transition from a fully tetrahedral (8*a*) to fully octahedral (16*c*) Li site occupancy can in principle occur.[47]

The experimental observation of a broad range of tetragonality in the transformed spinel (Figure 10) is inconsistent with a miscibility gap, allowing only two equilibrium compositions, and suggests a new phase diagram. We expect that as cation inversion is introduced into both the $LiMn_2O_4$ and $Li_2Mn_2O_4$ end-member phases, the miscibility gap will shrink in composition and temperature. The net volume change for the phase transformation will decrease as the solid-solution boundaries move together, and if the miscibility gap is suppressed below room temperature, a continuous variation in unit cell volume is possible. Note that, in $MgAl_2O_4$, another normal spinel, the unit cell volume increases by about 0.5% in partially disordered materials processed at low temperatures.[43] Partial cation inversion in the product $Li_2Mn_2O_4$ phase may also reduce its unit cell volume, thereby decreasing the volume change even if the phase transition remains first-order. These effects are expected to decrease the extent of mechanical damage occurring upon cycling across this composition region.

(2) Cation inversion may reduce the tetragonality because of collective JT distortion. The existence of reduced tetragonality in the lithiated spinel phase is also clearly from the experimental results. The question is whether it is due to cation inversion because local stresses within the nanodomain structure can also influence the tetragonality. The distribution of manganese ion valence between tetrahedral and octahedral sites and the JT distortion expected from each need to be taken into account. While the frequently cited JT distortion in manganese spinels is due to Mn^{3+} ions on octahedral sites, whose $t_{2g}^3e_g^1$ configuration induces tetragonal JT distortion of MnO_4 octahedra, other local JT distortions are also possible depending on the manganese valence and site.[48] In Table 4, we list the expected distortion for Mn^{4+}, Mn^{3+}, and Mn^{2+}, following the analysis of Dunitz and Orgel.[48]

In the partially inverse spinel, we may expect tetrahedral Mn to preferentially take on the 4+ valence when the average Mn valence is between 3+ and 4+ because of its smaller ionic size compared to that of Mn^{3+}. The spinel composition corresponding to this distribution can be written as follows:

$$(Li^{1+}_{x-i}Mn^{4+}_{i})_{8a}[Mn^{4+}_{2-i-x}Mn^{3+}_{x}Li_i]_{16d}O_4 \qquad (2)$$

The $e^2t_2^1$ configuration of Mn^{4+} on the 8*a* sites is expected to induce a JT distortion of individual MnO_4 tetrahedra that also results in $c/a > 1$ tetragonality.[48] If there is sufficient cation inversion, a collective tetragonal JT distortion due to distorted tetrahedra may even occur *before* the usual collective JT distortion occurs at $x = 1$. This additional distortion would not be expected to improve cycling stability.

Upon further lithiation beyond $x = 1$, the average manganese valence continues to decrease. Mn^{4+} on the octahedral sites will be oxidized to Mn^{3+} before those on the tetrahedral sites. However, at a limiting concentration determined by the extent of cation inversion, the tetrahedral manganese must finally be reduced. Two possibilities then arise, both of which would be expected to reduce the JT-induced $c/a > 1$ tetragonality of the transformed phase:

(a) Tetrahedral Mn^{4+} is reduced to Mn^{3+}. 8*a* site occupancy of Mn^{3+} is not unknown in spinel compounds, $NiMn_2O_4$ being one example.[49] The interesting characteristic of tetrahedral Mn^{3+} is that its $e^2t_2^2$ configuration induces a JT distortion of individual MnO_4 tetrahedra that is *opposite* to that induced by octahedral Mn^{3+} or tetrahedral Mn^{4+}, and which results in tetragonality with $c/a < 1$.[48] The $c/a > 1$ tetragonality due to octahedral Mn^{3+} could be partially or completely compensated by Mn^{3+} on 8*a* sites, depending on the extent of inversion.

(b) Mn^{3+} on the tetrahedral sites may disproportionate,[50] yielding tetrahedral Mn^{2+} (preferred due to covalency) and oxidizing an equal concentration of octahedral Mn^{3+} to Mn^{4+}:

$$(Mn^{3+})_{8a} + (Mn^{3+})_{16d} \rightarrow (Mn^{2+})_{8a} + (Mn^{4+})_{16d} \quad (3)$$

In this instance, diluting the concentration of octahedral JT Mn^{3+} ions with non-JT Mn^{4+} ions will also reduce the collective JT distortion. For instance, $Li_4Mn_5O_{12}$ ($Li[Mn_{1.67}Li_{0.33}]O_4$) spinel, which has a site occupancy that limits the Mn^{3+} concentration to one-half of the octahedral sites at the fully lithiated composition $Li_7Mn_5O_{12}$ ($Li_2[Mn^{4+}_{0.67}Mn^{3+}_{1.0}Li_{0.33}]O_4$), has a reduced JT-induced tetragonality ($c/a = 1.106$) compared to that of $Li_2Mn_2O_4$.[51]

The effect of aluminum doping on the tetragonality at the end of discharge also supports the basic idea that cation inversion reduces the tetragonal distortion. Al^{3+} is expected to preferentially occupy the tetrahedral sites over Mn^{4+} in a partially inverse spinel. The aluminum-doped samples studied here have the overall composition $Li_x(Al_{0.05}Mn_{0.95})O_2$, so that at most 5% of the total cation inversion can be accommodated by tetrahedral Al^{3+}. The concentration of tetrahedral Mn is correspondingly reduced, which should promote the $c/a > 1$ tetragonal distortion due to octahedral Mn^{3+}. The powder X-ray diffraction results showed that the dominant phase in transformed undoped *o*-$LiMnO_2$ at the end of discharge is cubic or very slightly tetragonal spinel (because of significantly broadened peaks, the two

(48) Dunitz, J. D.; Orgel, L. E. *J. Phys. Chem. Solids* **1957**, *3*, 20.
(49) Baudour, J. L.; Bouree, F.; Fremy, M. A.; Legros, R.; Rousset, A.; Gillot, B. *Physica B* **1992**, *180−181*, 97.
(50) Ceder, G., private communication.
(51) Thackeray, M. M.; de Kock, A.; Rossouw, M. H.; Liles, D. C.; Hoge, D.; Bittihn, R. *J. Electrochem. Soc.* **1992**, *139*, 363.

are difficult to distinguish),[40,41] whereas the major phase at the end of discharge in transformed *o*- and *m*-$Li_x(Al_{0.05}Mn_{0.95})O_2$ is clearly tetragonal spinel.[19,40]

Of the above mechanisms, all but one (JT distortion of tetrahedral Mn^{4+}) is qualitatively expected to contribute toward improved cycling stability. To understand the extent to which each occurs and its impact on cycling stability, a detailed study (experimental or theoretical) of the evolution of the cubic and tetragonal phases as a function of lithiation in a partially inverse spinel is required. Many of these questions could be answered through experiments on a substantially inverse $LiMn_2O_4$ that is *not* produced by electrochemical cycling. To date, however, the highest cation inversion reported in conventional $LiMn_2O_4$ spinel is <10%.[52]

5.2. Role of Antiphase and Ferroelastic Domains. While cation inversion may reduce the strains involved in the cubic → tetragonal phase transition, it does not avoid it entirely. This is evident from the fact that all of the cycled materials do contain some fraction of tetragonal phase. And the aluminum-doped samples have equally high reversible capacity and cycling stability (better at elevated temperatures[40]) than the undoped samples despite having greater tetragonality in the fully lithiated state. Here, we discuss the role of the ferroelastic domain structure in accommodating the transformation strains.

After an initial cycling transient during which Mn ions rearrange into the spinel ordering, subsequent cycling over the entire 2.0−4.4-V regime causes repetitive transitions between the cubic and tetragonal phases. Because of the cation inversion, we cannot say with certainty whether the transformation occurs with a continuous variation in volume and unit cell parameters or with a spontaneous strain because this depends on the phase diagram. However, it is clear from the microstructure (Figure 10) that individual nanodomains have changed in volume and shape relative to their neighbors. Because incoherent domain boundaries are evident only in the tetragonal phase, they clearly form during the cubic → tetragonal transformation. We propose *domain wall sliding* as the strain accommodation mechanism, illustrated in Figure 12. This is analogous to grain boundary sliding, which frequently occurs during the deformation of polycrystalline metals and ceramics as a mechanism for accommodating grain shape changes.[53] Like grain boundary sliding, domain wall sliding requires the presence of interfacial dislocations. In a comparison of Figures 8−10, it is apparent that the cubic → tetragonal transformation results in the creation of dislocations at virtually all domain walls. The edge component of several of these can be seen in the lattice fringe image in Figure 10. (From such images, we determined that on a volume basis the density of dislocations is extremely high, $\sim 2 \times 10^{12}$ cm^{-2}, which may be compared to a typical dislocation density of $\approx 10^9$ cm^{-2} in a cold-worked fcc metal.)

The very fine size of the nanodomains is undoubtedly also important to the successful accommodation of transformation strains. Note first that the mechanical properties of $LiMn_2O_4$ are expected to be typical of brittle ceramics. A Young's modulus of ≈150 GPa at room temperature, comparable to that for spinel ferrites such as Li−Cd or Mn−Zn ferrite,[54,55] seems reasonable. The fracture toughness is also expected to be typical of oxide ceramics (i.e., 2−4 MPa $m^{1/2}$). In a typical polycrystalline $LiMn_2O_4$ powder with a few micrometers particle size, it is not surprising that 5.6% differential volume expansion or a 16.3% change in tetragonality results in fracture. However, in Figure 10 we see that nearly cubic spinel with *c*/*a* as low as 1.03 and tetragonal spinel with *c*/*a* as high as 1.13 can coexist within a single parent crystallite of the transformed spinel. This indicates that the two-phase coexistence of $LiMn_2O_4$-type and $Li_2Mn_2O_4$-type spinel giving a flat 2.9-V plateau occurs at the nanodomain scale within a single oxide particle.

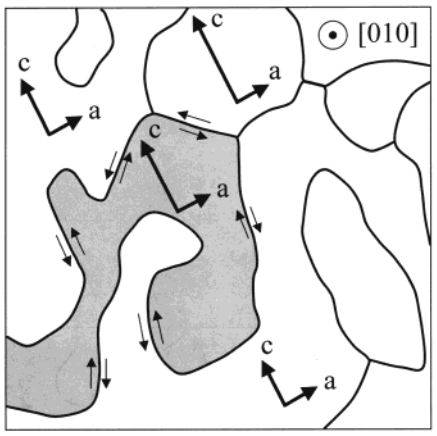

Figure 12. Domain wall sliding allows accommodation of the phase transformation strains as individually varying in their unit cell volume and tetragonality upon lithium insertion and removal.

Many examples exist in which polycrystalline ceramics are toughened and strengthened, or rendered more ductile, as a result of reduction in grain size. In undoped ZrO_2, the martensitic transformation from the tetragonal phase to the monoclinic phase (a special case of a ferroelastic transformation) occurring below 1440 K involves a shape change and a volume expansion of 4.7% at room temperature,[20] not too different from that for $LiMn_2O_4 \rightarrow Li_2Mn_2O_4$. This transformation is normally highly destructive; neither single crystals nor polycrystals of undoped ZrO_2 remain intact upon cooling through the transformation. However, in transformation-toughened zirconia alloys, reduction of the tetragonal zirconia crystallite size below 1 μm allows stabilization of the tetragonal phase to room temperature. The resulting materials in which transformation occurs only under stress are among the strongest and toughest ceramics known. Furthermore, at elevated temperatures where all atoms are to some extent mobile, the ductility of polycrystalline ceramics is known to increase as the grain size decreases. For certain combinations of grain size and doping, superplasticity can result.[56] The very fine ferroelastic domain size in the present transformed spinels suggests some unusual mechanical properties.

(52) Tarascon, J. M.; McKinnon, W. R.; Coowar, F.; Bowmer, T. N.; Amatucci, G.; Guyomard, D. *J. Electrochem. Soc.* **1994**, *141*, 1421.
(53) Sutton, A. P.; Balluffi, R. W. *Interfaces in Crystalline Materials*; Oxford University Press: Oxford, 1995.
(54) Ravinder, D. *J. Appl. Phys.* **1994**, *75*, 6121.
(55) Ravinder, D.; Alivelu Manga, T. *Mater. Lett.* **1998**, *37*, 51.
(56) Chen, I.-W.; Xue, L. A. *J. Am. Ceram. Soc.* **1990**, *73*, 2585.

5.3. Domain Texture Induced by Electromechanical Bias. As discussed in section 2, the cubic-to-tetragonal transformation produces three possible orientation states of the ferroelastic domains. If the phase transition were to occur uniformly in a particle, all three orientation states are equally probable, and a microtwinned structure resulting in zero macroscopic shape change (but nonzero volume change) is expected. This is not seen in the present materials. The absence of planar twin boundaries can be attributed to the high density of pre-existing APBs that become ferroelastic boundaries. The preferential orientation (texture) of the tetragonal nanodomains (Figure 11), on the other hand, is likely due to the imposed lithium concentration gradient. Because the molar volume varies with lithium concentration, the concentration gradient has an associated stress gradient (except when additional steps are taken to relax the stress). Thus, cycling is equivalent to carrying out the ferroelastic transformation under a mechanical bias. The formation of textured ferroelastic domains is expected.

We note that the process of charging and discharging an intercalation particle is analogous to the field-assisted ion-exchange strengthening of glass[57] in which mobile alkali ions are driven into the glass under an applied electric field to increase the surface molar volume and obtain surface compressive stresses. In the case of intercalation oxides, the reverse process of ion extraction also occurs, which results in surface tensile stress. As with other brittle solids, fracture should occur predominantly under tension, that is, during charging. Radial microcracking consistent with failure under tensile stress has been observed in cycled $LiCoO_2$ particles.[45,46]

5.4. Domain Formation in Other Intercalation Oxides. $LiCoO_2$ and $LiNiO_2$ are prototypical cathode oxides known for their good cycling behavior. Still, performance differences are observed between different preparations after hundreds of cycles. Table 2 shows that both antiphase and ferroelastic domains are possible upon charging to the composition $Li_{0.5}MO_2$, where a transformation to the monoclinic phase occurs. Compared to $LiMnO_2$, a key distinction is that the cation reordering giving rise to these domains can occur through the rearrangement of Li ions only. The high Li mobility suggests that transformation microstructures may be more difficult to observe. Cyclic transformation strains may nonetheless impact the long-term cycling behavior of these cathode materials. Partial spinel ordering has also been observed in cycled $LiCoO_2$,[46] which makes antiphase domain formation possible. Direct observations of extensively cycled $LiCoO_2$ or $LiNiO_2$ should reveal whether long-term stability is determined by cation disorder and domain formation.

(57) Bartholomew, R. F.; Garfinkel, H. M. Chemical Strengthening of Glass. In *Glass: Science and Technology*; Uhlmann, D. R., Kreidl, N. J., Eds.; Academic Press: New York, 1980; Vol. 5, pp 218−270.

VI. Conclusions

Electrochemical-cycling-induced phase transitions in lithium intercalation compounds can result in cation disorder as well as the formation of antiphase and ferroelastic domains. The crystallographically possible outcomes have been identified for several well-known lithium intercalation cathodes. The spinel transformation occurring when *o*- and *m*-$LiMnO_2$ are cycled through the $LiMn_2O_4$ composition has been experimentally studied and is shown to follow an irreversible multistage process:

(1) Partial cation inversion is retained as Mn ions undergo reordering into the spinel structure. Approximately 25% of the 8*a* tetrahedral sites are occupied by Mn after extensive electrochemical cycling.

(2) Concurrently, antiphase domains of several nanometer length scale are formed. The antiphase domain boundaries (APBs) remain coherent when the spinel phase is cubic.

(3) The APBs become incoherent, ferroelastic domain boundaries when further lithiation causes the cubic → tetragonal transformation.

(4) Cubic and tetragonal nanodomains can coexist within a single crystallite over the composition range $1 < x < 2$, providing the two-phase coexistence that gives a flat 2.9-V plateau. In predominantly tetragonal spinel, wide variations in tetragonality are observed between nanodomains.

The greater cycling stability of these transformed spinels compared to conventional $LiMn_2O_4$ is attributed primarily to ferroelastic accommodation of the transformation strains, although cation inversion may also contribute by reducing the volume change or tetragonality of the $LiMn_2O_4 \rightarrow Li_2Mn_2O_4$ transformation. A domain wall sliding mechanism is proposed for strain accommodation. Crystallographic considerations indicate that these antiphase and ferroelastic phase transitions can occur with other well-known lithium intercalation oxides. Understanding and improving cycling stability in lithium intercalation oxides therefore requires consideration of both crystal chemistry and microstructure.

Acknowledgment. We acknowledge funding and instrumentation in the Shared Experimental Facilities at MIT supported by NSF Grant 9400334-DMR.

CM000569Z